Localisation of Rayleigh–Bloch waves damps resonant loads on arrays of vertical cylinders

L. G. Bennetts[1], M. A. Peter[2,3] and F. Montiel[4]

[1]School of Mathematical Sciences, University of Adelaide, Adelaide, SA, Australia

[2]Institute of Mathematics, University of Augsburg, Augsburg, Germany

[3]Augsburg Centre for Innovative Technologies, University of Augsburg, Augsburg, Germany

[4]Department of Mathematics and Statistics, University of Otago, Dunedin, New Zealand

June 24, 2016

Abstract

Linear potential-flow theory is used to study the loads imposed on finite line arrays of rigid, bottom-mounted, surface-piercing, vertical cylinders by surface water waves. Perturbations in the locations of the cylinders are shown to damp the resonant loads experienced by the unperturbed array. A relationship is established between the damping and the phenomenon of Anderson localisation. Specifically, the Rayleigh–Bloch waves responsible for the resonant loads are shown to attenuate along the array when perturbations are introduced, resulting in localisation when the attenuation rate is sufficiently large with respect to the array length. Further, a new, efficient solution method for line arrays is introduced, capable of capturing the Rayleigh–Bloch wave modes supported by unperturbed arrays from the scattering characteristics of an individual cylinder.

1 Introduction

Maniar and Newman (1997) studied hydrodynamic loads imposed by surface water waves on columns supporting, for example, bridges or floating airports. They used a theoretical model based on linear potential-flow theory for the water, and modelled the columns as a long, finite straight-line array of equally spaced, bottom-mounted, surface-piercing cylinders with identical circular cross-sections. They found that cylinders within the array experience extreme, resonant loads at certain frequencies, with the strongest resonance imposing loads 35 times that of a cylinder in isolation, for cylinders in the middle of a 100-cylinder array. This occurred for a frequency just below the frequency at which a non-trivial solution exists for the related problem of a single cylinder in the centre of a channel with width equal to the cylinder spacing, and rigid walls on which the normal derivative of the potential vanishes (a Neumann trapped mode). They showed a weaker resonance occurs at a frequency just below the frequency at which a non-trivial solution exists for the cognate channel problem in which the potential vanishes on the channel walls (a Dirichlet trapped mode). These trapped modes may be interpreted as solutions of the infinite-array problem, existing in the absence of ambient incident wave forcing. Maniar and Newman (1997) argued that, although the trapped-mode solutions do not exist for a finite array, for long arrays incident waves excite large responses almost identical to the trapped modes around these frequencies — a phenomenon known as near-trapping — explaining the resonant loads. They found that near-trapping is strongest for head-on incidence (in the direction of the array), but is produced by any incident angle, up to symmetry requirements.

Evans and Porter (1999) established the Neumann trapped mode as the standing-wave limit of a so-called Rayleigh–Bloch wave — a trapped mode that propagates along an infinite array and decays exponentially away from it. For circular cylinders, Rayleigh–Bloch waves have been shown to exist for all values of cylinder radius and spacing, and all frequencies below the so-called cut-off, where

the Rayleigh–Bloch wave becomes a Neumann trapped mode. Below the cut-off, the Rayleigh–Bloch wavelength is shorter than the wavelength in the surrounding open water, so that it unequivocally cannot radiate energy away from the array. In this regime, incident waves cannot excite a Rayleigh–Bloch wave on an infinite array, as the incident wave imposes a quasi-periodicity on the wave field that is incompatible with the quasi-periodicity of the Rayleigh–Bloch wave. However, incident waves can excite Rayleigh–Bloch waves on arrays with ends, for example, semi-infinite arrays, where a Rayleigh–Bloch wave is generated at the end and propagates down the array, or finite arrays, where Rayleigh–Bloch waves are generated at both ends, propagating in both directions along the array.

Rayleigh–Bloch waves exist in other branches of wave science, for example, acoustics and electromagnetics, where they are sometimes known as edge, guided, surface or bound waves. Colquitt et al. (2015) recently developed low- and high-frequency homogenisation theories to calculate Rayleigh–Bloch waves in an elastic medium with an infinite array of voids. Their Introduction provides an up-to-date review of Rayleigh–Bloch waves in different phenomena.

Evans and Porter (1999) found that matching the Rayleigh–Bloch wavelength to the length of the array provides a better approximation of the resonant (near-trapping) frequency for the long, finite array than the frequency of the Neumann trapped mode. They showed that at this resonant frequency the wave-surface profile along the finite array almost exactly matches the profile of the Rayleigh-Bloch wave supported by the corresponding infinite array with an appropriately tuned amplitude, except in the vicinity of the array ends. Further, they showed that for cylinder-radius-to-spacing ratios greater than ~ 0.41, Rayleigh–Bloch waves exist that are antisymmetric with respect to the plane passing through the cylinder centres, in addition to the symmetric modes that exist for all ratios. Porter and Evans (1999) demonstrated existence of Rayleigh–Bloch waves for non-circular cylinders numerically, and Linton and McIver (2002) later proved existence for cylinders of arbitrary cross-sectional shape.

Linton et al. (2007) and Peter and Meylan (2007) independently developed similar solution methods for semi-infinite arrays forced by plane incident waves, by expressing the wave field as a superposition of the field supported by the corresponding infinite array under the same forcing, a Rayleigh–Bloch wave propagating down the array (when operating beneath the cut-off), and a decaying, circular wave generated at the array end. Thompson et al. (2008) extended this approach to give an efficient approximation method for long, finite arrays, in which Rayleigh–Bloch waves propagate in both directions along the array, and circular waves are generated at both ends but are assumed to have decayed sufficiently by the time they reach the opposite end that their influence is negligible. They showed that resonance in the middle of the array is due to a combination of (i) strong excitation of Rayleigh–Bloch waves, (ii) strong reflection of Rayleigh–Bloch waves at the ends of the array, and (iii) constructive interference of Rayleigh–Bloch waves following multiple reflections, all of which are satisfied just below the cut-off.

Motivated by the findings of Maniar and Newman (1997) and others, Kagemoto et al. (2002) used laboratory wave-tank experiments to study the wave field along an array of 50 identical, evenly-spaced cylinders with radius and spacing on the order 0.1 m, forced by plane waves at head-on incidence, and focussing on frequencies around the Neumann trapped mode. Measurements of free-surface elevations along the array were analysed, as proxies for the loads on the cylinders. They showed that the resonance is significantly smaller than the theoretical prediction and occurs towards the front of the array rather than in the middle. They attributed this to viscous dissipation on the cylinder surfaces, acknowledging that viscous effects would be far weaker at field scales.

The present study concerns the impacts of perturbing the cylinder locations from their regular arrangement on the excitation of resonant loads, with Fig. 1 acting as catalyst. It shows the frequency dependence of the maximum in-line load (the load in the direction of the array) produced by head-on incident waves on the 100-cylinder array considered in Fig. 2 of Maniar and Newman (1997), where the cylinder radius a and spacing d are such that $a/d = 0.25$. The perturbations are chosen randomly from uniform distributions, with the perturbation strength (later denoted ε) being half the magnitude of the maximum perturbation relative to the cylinder spacing. The results shown for the perturbed

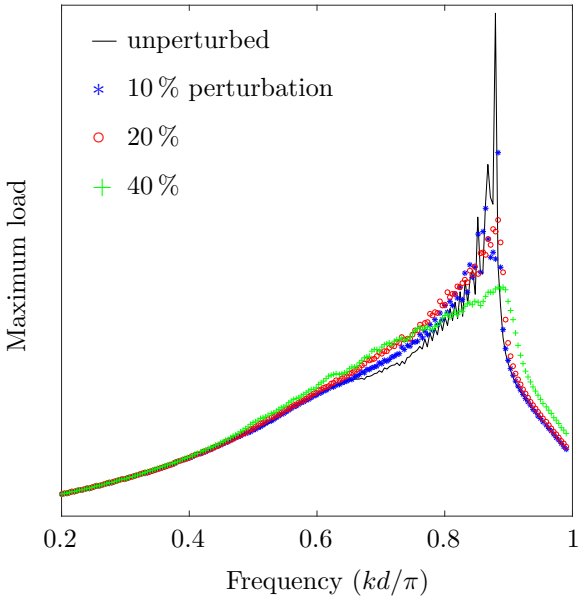

Figure 1: Maximum normalised in-line load on a 100-cylinder array produced by a plane incident wave at head-on incidence, with cylinder-radius-to-spacing ratio $a/d = 0.25$, for an unperturbed array ($\varepsilon = 0$, –), and the means of ensembles of 100 randomly generated realisations of perturbed arrays, using relative perturbation strength of 10 % ($\varepsilon = 0.1$, ∗), 20 % ($\varepsilon = 0.2$, ∘), and 40 % ($\varepsilon = 0.4$, +).

arrays are means of ensembles of 100 randomly generated realisations of the array. The loads are normalised following Maniar and Newman (1997), as defined in § 2, and no attempt has been made to sample the frequency range in order to capture the resonance exactly. The results are for illustrative purposes only and the scale of the loads are omitted accordingly.

The loads for the unperturbed array display the strongest resonance, associated with the Neumann trapped mode, as identified by Maniar and Newman (1997) and others. The frequency range shown extends just beyond the cut-off at frequency $kd/\pi \approx 0.88574$, omitting the weaker resonance associated with the Dirichlet trapped mode. As in Evans and Porter (1999), Thompson et al. (2008) and others, the focus of this investigation will be on frequencies around the strongest resonance. Perturbations significantly damp this resonance, with the damping increasing as the perturbation strength increases. Maximum loads away from the resonance are relatively unaffected by perturbations.

In many other situations involving wave propagation through some medium, random perturbations in the medium suppress wave propagation, spatially localising wave energy to a vicinity of their source — a phenomenon known as Anderson localisation (see the book by Sheng, 2006). Localisation can be identified as exponential attenuation of the wave through the medium, for which, in the absence of perturbations, the wave would propagate without loss of intensity. It has been discovered, mainly theoretically but also experimentally, for classical waves in many contexts, including structural acoustics (Hodges and Woodhouse, 1983), ultrasonics (Weaver, 1990) and optics (Berry and Klein, 1997).

Guazzelli and Guyon (1983) predicted one-dimensional shallow-water waves would be localised by random perturbations in the bathymetry. Experimental evidence of this was provided by Belzons et al. (1988), using a wave tank with random steps in its floor, and a corresponding theoretical model, based on linear theory, developed by Devillard et al. (1988). Bennetts et al. (2015) showed that random bathymetry is unlikely to induce localisation in finite-depth water, for small-amplitude perturbations.

Bennetts and Squire (2012) proposed a two-dimensional model (one-dimensional waves plus a depth dimension) of water-wave localisation produced by an array of sea ice floes (thin, floating bod-

ies), in which wave phases are randomised between adjacent bodies, based on the theory of Berry and Klein (1997). Peter and Meylan (2009) developed a cognate three-dimensional model (two-dimensional waves), in which floe locations are perturbed around a periodic arrangement. They showed the predicted attenuation rates are comparable to those measured during field experiments in a mid-range frequency band.

Here, random perturbations in the locations of cylinders in the line array are shown to localise Rayleigh–Bloch waves, within the framework of linear potential-flow theory, leading to the damping of resonant loads observed in Fig. 1. To the authors' knowledge, localisation of Rayleigh–Bloch modes has not been investigated in any context previously. As part of the study, a new solution method is introduced for line arrays, adapted from the method outlined by Montiel et al. (2015, 2016) for wave propagation through large, finite arrays of scatterers/floating bodies. For line arrays of cylinders, it allows the wave field to be constructed recursively from the scattering characteristics of the individual cylinders, so that ensembles of order 100 can be constructed efficiently for arrays containing order 100 cylinders and over a large number of frequencies. Moreover, the Rayleigh–Bloch wave modes supported by unperturbed arrays are identified from the scattering characteristics of individual cylinders, without evaluating slowly convergent Schlömilch series, as necessitated by standard interaction theory. The key challenge is then to extract perturbed Rayleigh–Bloch wave numbers from the overall wave fields, and this is achieved by (i) using Rayleigh–Bloch waves rather than plane waves as forcing, and (ii) combining wave fields forced by Rayleigh–Bloch waves propagating in opposite directions for each individual realisation of the perturbed array. Weak perturbations are shown predominantly to increase the Rayleigh–Bloch wavelengths. Stronger perturbations cause them to attenuate along the array, damping the resonance and shifting the maximum load to the front of the array.

2 Preliminaries

Consider a three-dimensional domain containing water and a line array of N bottom-mounted surface-piercing cylinders. The volume of water is of infinite horizontal extent and finite depth. Geometrical locations in the domain are defined using the Cartesian coordinate system (x, y, z). The coordinate (x, y) defines horizontal locations. The coordinate z defines vertical locations. It points upwards and its origin coincides with the equilibrium water surface. The volume of water is bounded below by a flat impermeable bed at $z = -h$, and above by its interface with the atmosphere, which is free to move when the water is in motion.

The cylinders are identical and have radius $a > 0$. They extend throughout the water column and high enough above the water surface that waves do not wash over their upper surfaces. In the absence of positional disorder, the cylinders are regularly spaced along the x-axis. The distance between the geometrical centres of adjacent cylinders in the horizontal plane is denoted $d > 2a$. The cylinders are indexed $1, \ldots, N$ according to their ordering along the x-axis. The horizontal coordinates of the cylinder centres are denoted

$$(x_n, y_n) = (x_0 + (n-1)d, 0) \qquad \text{for} \quad n = 1, \ldots, N. \tag{1}$$

The horizontal regions occupied by the cylinders are denoted

$$\mathcal{C}_n = \{(x, y) : (x - x_n)^2 + (y - y_n)^2 < a^2\} \qquad \text{for} \quad n = 1, \ldots, N, \tag{2}$$

with boundaries

$$\partial\mathcal{C}_n = \{(x, y) : (x - x_n)^2 + (y - y_n)^2 = a^2\} \qquad \text{for} \quad n = 1, \ldots, N. \tag{3}$$

Figure 2 shows schematics of the geometry for the unperturbed array.

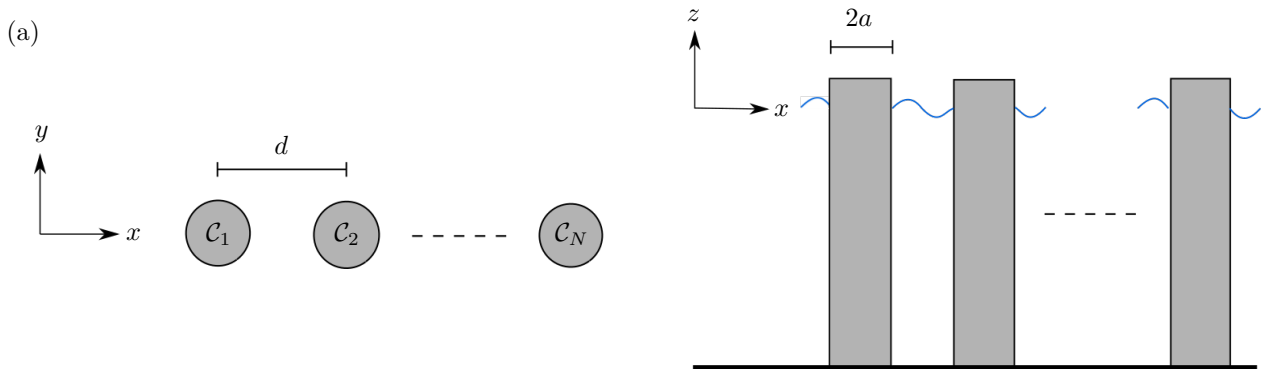

Figure 2: Schematics of the unperturbed geometry: (a) plan view; and (b) cross-sectional side view.

Under the usual assumptions of linear water-wave theory, the water is modelled as being homogeneous, inviscid, incompressible and in irrotational motion. Moreover, time-harmonic motions are imposed, for a prescribed angular frequency ω. Thus, the water velocity field is defined via

$$\mathrm{Re}\left\{\frac{g}{\mathrm{i}\omega}(\partial_x,\partial_y,\partial_z)\Phi(x,y,z)\mathrm{e}^{-\mathrm{i}\omega t}\right\}, \tag{4}$$

where Φ is a reduced (complex-valued, time-independent) velocity potential, $g \approx 9.81\,\mathrm{m\,s^{-2}}$ is the constant of gravitational acceleration, and $\partial_\bullet \equiv \partial/\partial\bullet$ denotes a partial derivative.

The velocity potential satisfies Laplace's equation throughout the water domain

$$\nabla^2\Phi + \partial_z^2\Phi = 0 \qquad \text{for} \quad (x,y) \in \Omega \quad \text{and} \quad -h < z < 0, \tag{5a}$$

where $\nabla \equiv (\partial_x, \partial_y)$ and $\Omega = \{(x,y) : x,y \in \mathbb{R} \text{ and } (x,y) \notin \overline{\mathcal{C}}_n \text{ for } n = 1,\dots,N\}$ denotes the horizontal region occupied by the water (over bars denote closed regions). On the bed it satisfies the no-flux condition

$$\partial_z\Phi = 0 \qquad \text{on} \quad z = -h \quad \text{for} \quad (x,y) \in \Omega, \tag{5b}$$

and on the wetted surfaces of the cylinders, it satisfies the no-flux condition

$$\partial_{r^{(n)}}\Phi = 0 \qquad \text{on} \quad \partial\mathcal{C}_n \times (-h,0) \quad \text{for} \quad n = 1,\dots,N, \tag{5c}$$

where $r^{(n)}$ is outward-pointing normal to $\mathcal{C}_n$ (the radial coordinate relative to cylinder n, defined in § 3). At the linearised water–atmosphere interface it satisfies the free-surface condition

$$\partial_z\Phi = \kappa\Phi \qquad \text{on} \quad z = 0 \quad \text{for} \quad (x,y) \in \Omega, \tag{5d}$$

where $\kappa = \omega^2/g$.

An ambient incident wave field forces a non-trivial solution. Its velocity potential is denoted

$$\Phi_{\mathrm{am}}(x,y,z) = \frac{\phi_{\mathrm{am}}(x,y)\cosh\left(k(z+h)\right)}{\cosh(kh)} \tag{6a}$$

where, for a unit-amplitude plane incident wave propagating in direction ψ_{am} with respect to the positive x-axis,

$$\phi_{\mathrm{am}}(x,y) \equiv \varphi(x,y:\psi_{\mathrm{am}}) = \mathrm{e}^{\mathrm{i}k(x\cos\psi_{\mathrm{am}} + y\sin\psi_{\mathrm{am}})}. \tag{6b}$$

The wave number k is the unique positive real root of the dispersion relation

$$k\tanh(kh) = \kappa. \tag{7}$$

The vertical structure of the incident wave field supports propagating wave motions. The Sommerfeld radiation condition is applied in the far field to the total scattered wave field, $\Phi - \Phi_{\text{am}}$, i.e.

$$\sqrt{r}(\partial_r - \mathrm{i}k)(\Phi - \Phi_{\text{am}}) \to 0 \qquad \text{as} \quad r \to \infty, \tag{8}$$

where $r = \sqrt{x^2 + y^2}$ is the radial coordinate of the horizontal plane, holds uniformly in the azimuthal coordinate $\theta = \arctan(y/x)$ ($\theta = \pm\pi/2$ for $x = 0$ and $\pm y > 0$).

Due to uniformity of the geometry in the vertical dimension, the velocity potential inherits the vertical structure of the incident wave field, i.e.

$$\Phi(x, y, z) = \frac{\phi(x, y)\cosh\left(k(z + h)\right)}{\cosh(kh)}. \tag{9}$$

This means that interactions between the incident wave and the array do not excite evanescent waves. Velocity potential (9) automatically satisfies the bed condition (5b) and the free-surface condition (5d). It reduces Laplace's equation (5a) in the volume of water to the two-dimensional Helmholtz equation

$$\nabla^2\phi + k^2\phi = 0 \qquad \text{for} \quad (x, y) \in \Omega, \tag{10a}$$

and the cylinder surface conditions (5c) to

$$\partial_{r^{(n)}}\phi = 0 \qquad \text{on} \quad \partial\mathcal{C}_n \quad \text{for} \quad n = 1, \ldots, N. \tag{10b}$$

The Sommerfeld radiation condition (8) applies to the functions in the horizontal plane, i.e.

$$\sqrt{r}(\partial_r - \mathrm{i}k)(\phi - \phi_{\text{am}}) \to 0 \qquad \text{as} \quad r \to \infty. \tag{10c}$$

For a cylinder centred at the origin of the horizontal plane, $(x_n, y_n) = (0, 0)$, following Maniar and Newman (1997), the normalised in-line load shown in Fig. 1 is defined in terms of the velocity potential, as the magnitude of

$$F_x = \frac{\tanh(ka)}{ka}\int_{-\pi}^{\pi} \phi|_{r=a}\cos(\theta)\ \mathrm{d}\theta. \tag{11}$$

Positional disorder is introduced into the problem via random perturbations in the locations of the cylinders. The perturbed locations of the centres of cylinders are denoted

$$(x_n, y_n) = (x_0 + (n - 1)d, 0) + \mathbf{p}_n \qquad \text{for} \quad n = 1, \ldots, N. \tag{12}$$

A parameter ε is used to control the perturbation strength, with the perturbation vectors expressed as

$$\mathbf{p}_n = \varepsilon d(\mu_n, \nu_n) \qquad \text{for} \quad n = 1, \ldots, N, \tag{13}$$

where μ_n and ν_n are randomly selected from uniform distributions over the interval $[-0.5, 0.5]$. The perturbation strength is chosen to be small enough that the cylinders cannot overlap, i.e. $\varepsilon < 1 - 2a/d$. Figure 3 shows a schematic of the perturbed geometry.

3 Solution method

3.1 Scattering by a single cylinder

Consider the subregion of the horizontal plane

$$\Omega_n = \{(x, y) : x_{n-} < x < x_{n+} \text{ and } y \in \mathbb{R}\}, \tag{14}$$

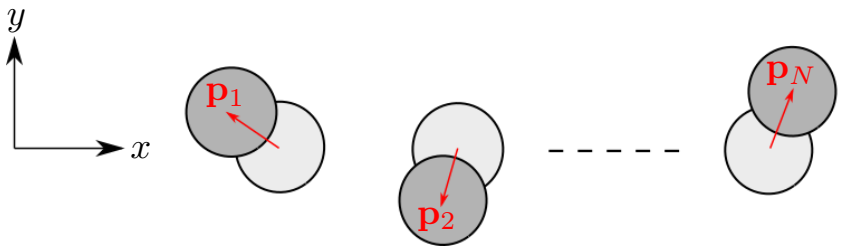

Figure 3: Schematic plan view of the perturbed geometry.

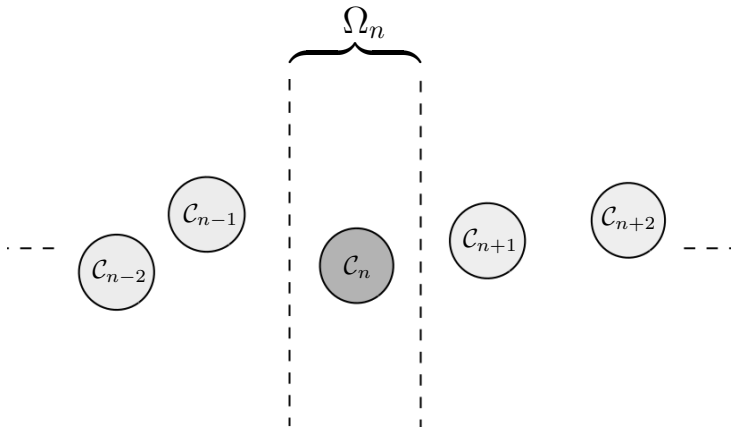

Figure 4: Subregion Ω_n containing cylinder $\mathcal{C}_n$, as defined in Eqn. (14).

where the limits $x_{n\pm}$ are chosen so that it contains cylinder n only, i.e. $x_{n-1}+a<x_{n-}<x_n-a$ and $x_n+a<x_{n+}<x_{n+1}-a$, and $x_{n+}=x_{(n+1)-}$ for $n=1,\ldots,N-1$. Fig. 4 shows an example schematic of the subregion.

In this region, the velocity potential is decomposed as

$$\phi\equiv\phi^{(n)}=\phi^{(n)}_{\mathrm{in}}+\phi^{(n)}_{\mathrm{sc}}\quad\text{for}\quad(x,y)\in\Omega_n, \tag{15}$$

where $\phi^{(n)}_{\mathrm{sc}}$ represents a local scattered wave field, and $\phi^{(n)}_{\mathrm{in}}$ represents a local incident wave field, which consists of the ambient incident wave field and the wave fields scattered by all other cylinders. For presentational convenience, the domain of the potentials extends over the entire subregion Ω_n, including the disc $\mathcal{C}_n$ occupied by the cylinder via analytic continuation. In this sense, the cylinder is considered to be a point source acting at its centre (x_n,y_n) (formally omitting the source point from the domain).

The standard expressions for the incident and scattered fields are the Fourier–Bessel series

$$\phi^{(n)}_{\mathrm{in}}=\sum_{m=-\infty}^{\infty}a^{(n)}_m\mathrm{J}_m(kr^{(n)})\mathrm{e}^{\mathrm{i}m\theta^{(n)}}\qquad\text{and}\qquad\phi^{(n)}_{\mathrm{sc}}=\sum_{m=-\infty}^{\infty}b^{(n)}_m\mathrm{H}_m(kr^{(n)})\mathrm{e}^{\mathrm{i}m\theta^{(n)}}, \tag{16}$$

where J_m and H_m ($m\in\mathbb{Z}$) are, respectively, the Bessel and Hankel functions of the first kind of order m, and

$$r^{(n)}=\sqrt{(x-x_n)^2+(y-y_n)^2}\qquad\text{and}\qquad\theta^{(n)}=\arctan\left(\frac{y-y_n}{x-x_n}\right), \tag{17}$$

are, respectively, the radial and azimuthal coordinates with respect to the centre of the cylinder. The coefficients $a_m^{(n)}$ and $b_m^{(n)}$ ($m \in \mathbb{Z}$) are unknown at this juncture. The cylinder boundary condition (10b) relates the incident and scattered coefficients, with

$$b_m^{(n)} = Z_m a_m^{(n)} \qquad \text{for} \quad m \in \mathbb{Z}, \tag{18}$$

where $Z_m = -\mathrm{J}'_m(ka)/\mathrm{H}'_m(ka)$ (e.g. Martin, 2006). The Fourier modes are decoupled due to axisymmetry of the boundary. For computations, the infinite series are truncated, so that $|m| \leq M \in \mathbb{N}$, where M is chosen to gain desired accuracy. The value $M = 5$ is used for the results presented in § 4 and § 5.

3.2 Reflection and transmission kernels

Let the local incident wave field be a unit amplitude plane wave with direction ψ, i.e. $\phi_{\mathrm{in}}^{(n)}(x, y) = \varphi(x, y : \psi)$. This incident wave field has the Fourier–Bessel series representation

$$\varphi(x, y : \psi) = \varphi_n(\psi) \sum_{m=-\infty}^{\infty} \mathrm{e}^{\mathrm{i}m(\pi/2-\psi)} \mathrm{J}_m(kr^{(n)}) \mathrm{e}^{\mathrm{i}m\theta^{(n)}}, \qquad \text{where} \qquad \varphi_n(\psi) \equiv \varphi(x_n, y_n : \psi) \tag{19}$$

provides the phase change necessitated by the cylinder being centred away from the origin. The corresponding scattered wave field is $\phi_{\mathrm{sc}}^{(n)}(x, y) \equiv \varphi_{\mathrm{sc}}^{(n)}(x, y : \psi)$, where

$$\varphi_{\mathrm{sc}}^{(n)}(x, y : \psi) = \varphi_n(\psi) \sum_{m=-\infty}^{\infty} Z_m \mathrm{e}^{\mathrm{i}m(\pi/2-\psi)} \mathrm{H}_m(kr^{(n)}) \mathrm{e}^{\mathrm{i}m\theta^{(n)}} \tag{20a}$$

$$= \int_{\Gamma_\mp} \left\{ \frac{\varphi_n(\psi)}{\pi \varphi_n(\chi)} \sum_{m=-\infty}^{\infty} Z_m \mathrm{e}^{\mathrm{i}m(\chi-\psi)} \right\} \varphi(x, z : \chi) \, \mathrm{d}\chi \quad \text{for } \pm(x - x_n) \geq 0, \tag{20b}$$

with integration contours

$$\Gamma_- = \{-\pi/2 + \mathrm{i}\gamma : \gamma \in \mathbb{R}^+\} \cup \{\gamma \in \mathbb{R} : -\pi/2 \leq \gamma \leq \pi/2\} \cup \{\pi/2 - \mathrm{i}\gamma : \gamma \in \mathbb{R}^+\}, \tag{21}$$

and $\Gamma_+ = \Gamma_- + \pi$. The grey curve in Fig. 5(a) shows the contour Γ_- in the complex plane.

On the real branches of $\Gamma_\pm$, the function φ defines waves that propagate rightwards for Γ_- and leftwards for Γ_+. On the complex branches of $\Gamma_\pm$, it defines waves that decay rightwards for Γ_- and leftwards for Γ_+. Therefore, Eqn. (20b) expresses the scattered wave field as integrals of waves propagating/decaying leftwards on the left-hand side of the source, and propagating/decaying rightwards on its right-hand side. It is derived using the Sommerfeld integral representation for the Hankel functions (Sommerfeld, 1949, § 19), in the form

$$\mathrm{H}_m(kr)\mathrm{e}^{\mathrm{i}m\theta} = \frac{1}{\pi} \int_{\Gamma_\mp} \mathrm{e}^{\mathrm{i}m(\chi-\pi/2)} \varphi(x, y : \chi) \, \mathrm{d}\chi \qquad \text{for} \quad \pm x \geq 0. \tag{22}$$

The incident wave field is generalised to

$$\phi_{\mathrm{in}}^{(n)} = \phi_{\mathrm{in}-}^{(n)} + \phi_{\mathrm{in}+}^{(n)} \qquad \text{where} \qquad \phi_{\mathrm{in}\pm}^{(n)} = \int_{\Gamma_\pm} A_\pm^{(n)}(\chi) \varphi(x, y : \chi) \, \mathrm{d}\chi, \tag{23}$$

by superposing plane incident potentials, φ, over directions $\psi \in \Gamma_\pm$, weighted by amplitude functions $A_\pm^{(n)}$. (Note, plane decaying waves are included by choosing the direction ψ to be on the appropriate complex branch of $\Gamma_\pm$.) The potential $\phi_{\mathrm{in}-}^{(n)}$ represents rightward propagating/decaying waves incident from the left-hand boundary of Ω_n, and $\phi_{\mathrm{in}+}^{(n)}$ represents leftward propagating/decaying waves incident

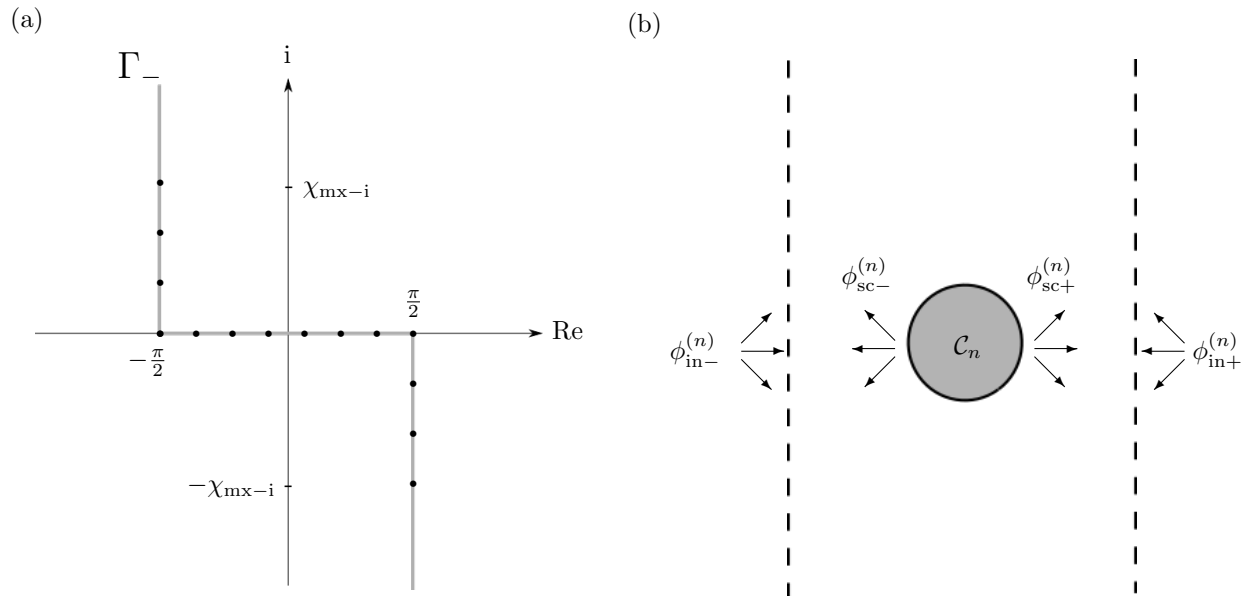

Figure 5: (a) Integration contour Γ_- (–) in the complex plane, as defined in Eqn. (21), and sampled points used for numerical approximation (•), as defined in Eqn. (34). (b) Incident and scattered fields, as defined in Eqns. (23) and (24), respectively.

from the right-hand boundary of Ω_n. Fig. 5(b) illustrates the incident wave fields (23) and the corresponding scattered wave fields defined in Eqn. (24) below.

For the generalised incident wave field (23), the scattered wave field is expressed as

$$\phi^{(n)}_{\mathrm{sc}} \equiv \phi^{(n)}_{\mathrm{sc}\pm} = \int_{\Gamma_\mp} \tilde{B}^{(n)}_{\pm}(\chi)\varphi(x, y : \chi)\ \mathrm{d}\chi \qquad \text{for} \quad \pm\,(x - x_n) \geq 0, \tag{24}$$

where the $\tilde{B}^{(n)}_{\pm}$ are scattered amplitude functions. The generalised scattered wave field is obtained by superposing scattered wave fields produced by plane incident waves, i.e.

$$\phi^{(n)}_{\mathrm{sc}}(x, y) = \int_{\Gamma_-} A^{(n)}_{-}(\psi)\varphi^{(n)}_{\mathrm{sc}}(x, y : \psi)\ \mathrm{d}\psi + \int_{\Gamma_+} A^{(n)}_{+}(\psi)\varphi^{(n)}_{\mathrm{sc}}(x, y : \psi)\ \mathrm{d}\psi, \tag{25}$$

which, upon substituting the integral representation (24) for the scattered wave field on the left-hand side of Eqn. (25) and expression (20b) for $\varphi^{(n)}_{\mathrm{sc}}$ on its right-hand side, after manipulations, gives the scattered amplitude functions

$$\tilde{B}^{(n)}_{\pm}(\chi) = \int_{\Gamma_-} \left\{ \frac{\varphi_n(\psi)}{\pi\varphi_n(\chi)} \sum_{m=-\infty}^{\infty} Z_m \mathrm{e}^{\mathrm{i}m(\chi-\psi)} \right\} A^{(n)}_{-}(\psi)\ \mathrm{d}\psi \tag{26a}$$

$$+ \int_{\Gamma_+} \left\{ \frac{\varphi_n(\psi)}{\pi\varphi_n(\chi)} \sum_{m=-\infty}^{\infty} Z_m \mathrm{e}^{\mathrm{i}m(\chi-\psi)} \right\} A^{(n)}_{+}(\psi)\ \mathrm{d}\psi. \tag{26b}$$

The total wave field, $\phi^{(n)}$, is decomposed into fields propagating/decaying rightwards and leftwards on the left- and right-hand sides of the source via the integral representations

$$\phi^{(n)} = \int_{\Gamma_\pm} A^{(n)}_{\pm}(\chi)\varphi(x, y : \chi)\ \mathrm{d}\chi + \int_{\Gamma_\mp} B^{(n)}_{\pm}(\chi)\varphi(x, y : \chi)\ \mathrm{d}\chi \qquad \text{for} \quad \pm\,(x - x_n) \geq 0. \tag{27}$$

where $B_{\pm}^{(n)} = A_{\mp}^{(n)} + \tilde{B}_{\pm}^{(n)}$ represent outgoing amplitude functions (with respect to the source). The $A_{\pm}^{(n)}$ are, accordingly, referred to as incoming amplitude functions. The outgoing amplitude functions are expressed in terms of the incoming amplitude functions using the scattering relations

$$B_{-}^{(n)}(\chi) = \int_{\Gamma_-} R^{(n)}(\chi:\psi) A_{-}^{(n)}(\psi)\ \mathrm{d}\psi + \int_{\Gamma_+} T^{(n)}(\chi:\psi) A_{+}^{(n)}(\psi)\ \mathrm{d}\psi \tag{28a}$$

$$\text{and} \quad B_{+}^{(n)}(\chi) = \int_{\Gamma_-} T^{(n)}(\chi:\psi) A_{-}^{(n)}(\psi)\ \mathrm{d}\psi + \int_{\Gamma_+} R^{(n)}(\chi:\psi) A_{+}^{(n)}(\psi)\ \mathrm{d}\psi. \tag{28b}$$

Here, $R^{(n)}$ and $T^{(n)}$ are, respectively, reflection and transmission kernels, which are defined by

$$R^{(n)}(\chi:\psi) = \frac{\varphi_n(\psi)}{\pi\varphi_n(\chi)} \sum_{m=-\infty}^{\infty} Z_m \mathrm{e}^{\mathrm{i}m(\chi-\psi)} \tag{29a}$$

$$\text{and} \qquad T^{(n)}(\chi:\psi) = \delta(\chi-\psi) + \frac{\varphi_n(\psi)}{\pi\varphi_n(\chi)} \sum_{m=-\infty}^{\infty} Z_m \mathrm{e}^{\mathrm{i}m(\chi-\psi)}. \tag{29b}$$

They determine the outgoing amplitude response in direction χ due to an incoming amplitude forcing in direction ψ.

3.3 Multiple cylinders and numerical implementation

The phase-shifted amplitude functions

$$\hat{A}_{\pm}^{(n)}(\chi) = \mathrm{e}^{\mathrm{i}kx_{n\pm}\cos(\chi)} A_{\pm}^{(n)}(\chi) \quad \text{and} \quad \hat{B}_{\pm}^{(n)}(\chi) = \mathrm{e}^{\mathrm{i}kx_{n\pm}\cos(\chi)} B_{\pm}^{(n)}(\chi), \tag{30}$$

are used to facilitate analysis of interactions between subregions. They normalise the phase of the waves to the left- or right-hand side of the region, i.e.

$$\phi^{(n)} = \int_{\Gamma_\pm} \hat{A}_{\pm}^{(n)}(\chi)\hat{\varphi}_{\pm}^{(n)}(x,y:\chi)\ \mathrm{d}\chi + \int_{\Gamma_\mp} \hat{B}_{\pm}^{(n)}(\chi)\hat{\varphi}_{\pm}^{(n)}(x,y:\chi)\ \mathrm{d}\chi \qquad \text{for} \quad \pm(x-x_n) > 0, \tag{31}$$

where $\hat{\varphi}_{n\pm} = \mathrm{e}^{\mathrm{i}k\{(x-x_{n\pm})\cos\psi + y\sin\psi)\}}$. They are related to one other via

$$\hat{B}_{-}^{(n)}(\chi) = \int_{\Gamma_-} \hat{R}_{-}^{(n)}(\chi:\psi)\hat{A}_{-}^{(n)}(\psi)\ \mathrm{d}\psi + \int_{\Gamma_+} \hat{T}_{+}^{(n)}(\chi:\psi)\hat{A}_{+}^{(n)}(\psi)\ \mathrm{d}\psi \tag{32a}$$

$$\text{and} \quad \hat{B}_{+}^{(n)}(\chi) = \int_{\Gamma_-} \hat{T}_{-}^{(n)}(\chi:\psi)\hat{A}_{-}^{(n)}(\psi)\ \mathrm{d}\psi + \int_{\Gamma_+} \hat{R}_{+}^{(n)}(\chi:\psi)\hat{A}_{+}^{(n)}(\psi)\ \mathrm{d}\psi, \tag{32b}$$

where the reflection and transmission kernels, $\hat{R}_{\pm}^{(n)}$ and $\hat{T}_{\pm}^{(n)}$, are

$$\hat{R}_{\pm}^{(n)}(\chi:\psi) = \mathrm{e}^{\mathrm{i}kx_{n\pm}(\cos\chi-\cos\psi)} R^{(n)}(\chi:\psi) \quad \text{and} \quad \hat{T}_{\pm}^{(n)}(\chi:\psi) = \mathrm{e}^{\mathrm{i}k(x_{n\mp}\cos\chi - x_{n\pm}\cos\psi)} T^{(n)}(\chi:\psi), \tag{33}$$

respectively.

For numerical implementation, the complex branches of the contour Γ_-, and, hence, Γ_+, are truncated, with the magnitude of the imaginary parts restricted to being less than or equal to a prescribed value $\chi_{\mathrm{mx-i}} \in \mathbb{R}^+$. Further, the truncated contours are sampled, with the real and complex branches sampled at regular points, respectively. The sampled points of Γ_- are denoted

$$\psi_j = -\frac{\pi}{2} + \mathrm{i}\chi_{\mathrm{mx-i}}\left(1 - \frac{j-1}{J_{\mathrm{i}}-1}\right) \qquad \text{for} \quad j = 1,\ldots,J_{\mathrm{i}}-1, \tag{34a}$$

$$\psi_j = -\frac{\pi}{2} + \frac{\pi(j - J_\mathrm{i})}{J_\mathrm{r}} \qquad \text{for} \quad j = J_\mathrm{i}, \ldots, J_\mathrm{i} + J_\mathrm{r}, \tag{34b}$$

$$\text{and} \qquad \psi_j = \frac{\pi}{2} - \frac{\mathrm{i}\chi_{\mathrm{mx-i}}(j - J_\mathrm{i} - J_\mathrm{r})}{J_\mathrm{i} - 1} \qquad \text{for} \quad j = J_\mathrm{i} + J_\mathrm{r} + 1, \ldots, 2J_\mathrm{i} + J_\mathrm{r} - 1. \tag{34c}$$

The truncation limit of the complex branches, $\chi_{\mathrm{mx-i}}$, and the number of samples of the real and complex branches, J_r and J_i, are chosen to achieve a desired level of accuracy. The values $\chi_{\mathrm{mx-i}} = 2$, $J_\mathrm{r} = 100$ and $J_\mathrm{i} = 101$ are used for the results presented in § 4 and § 5. The black bullets on Fig. 5(a) are an example of the truncated and sampled version of the contour Γ_-.

Therefore, the operator relations given in Eqns. (32) are approximated by the array relations

$$\hat{\mathbf{b}}_-^{(n)} = \hat{\mathbf{R}}_-^{(n)} \hat{\mathbf{a}}_-^{(n)} + \hat{\mathbf{T}}_+^{(n)} \hat{\mathbf{a}}_+^{(n)} \qquad \text{and} \qquad \hat{\mathbf{b}}_+^{(n)} = \hat{\mathbf{T}}_-^{(n)} \hat{\mathbf{a}}_-^{(n)} + \hat{\mathbf{R}}_+^{(n)} \hat{\mathbf{a}}_+^{(n)}, \tag{35}$$

where the amplitude vectors $\hat{\mathbf{a}}_\pm^{(n)}$ and $\hat{\mathbf{b}}_\pm^{(n)}$ have entries

$$\{\hat{\mathbf{a}}_\pm^{(n)}\}_j = \hat{A}_\pm^{(n)}(\chi_j) \quad \text{and} \quad \{\hat{\mathbf{b}}_\pm^{(n)}\}_j = \hat{B}_\pm^{(n)}(\chi_j) \qquad \text{for} \quad j = 1, \ldots, 2J_\mathrm{i} + J_\mathrm{r} - 1, \tag{36}$$

and the matrices $\hat{\mathbf{R}}_\pm^{(n)}$ and $\hat{\mathbf{T}}_\pm^{(n)}$ have entries

$$\{\hat{\mathbf{R}}_\pm^{(n)}\}_{i,j} = w_i \hat{R}_\pm^{(n)}(\chi_j : \chi_i) \quad \text{and} \quad \{\hat{\mathbf{T}}_\pm^{(n)}\}_{i,j} = w_i \hat{T}_\pm^{(n)}(\chi_j : \chi_i) \qquad \text{for} \quad i, j = 1, \ldots, 2J_\mathrm{i} + J_\mathrm{r} - 1. \tag{37}$$

These matrices combine the reflection and transmission kernels and numerical integration, where w_i ($i = 1, \ldots, 2J_\mathrm{i} + J_\mathrm{r} - 1$) denote the quadrature weights — a composite trapezoidal rule is used for numerical calculations in § 4 and § 5.

For $p \le q$, the region $\Omega_{p,q}$ is defined as the union of regions Ω_p to Ω_q, i.e.

$$\Omega_{p,q} = \left(\bigcup_{n=p}^{q} \overline{\Omega}_n \right)^\mathrm{o}, \tag{38}$$

where the superscript o denotes the open set. Let $\hat{\mathbf{R}}_\pm^{(p,q)}$ and $\hat{\mathbf{T}}_\pm^{(p,q)}$ denote the reflection and transmission matrices for this region, i.e.

$$\hat{\mathbf{b}}_-^{(p)} = \hat{\mathbf{R}}_-^{(p,q)} \hat{\mathbf{a}}_-^{(p)} + \hat{\mathbf{T}}_+^{(p,q)} \hat{\mathbf{a}}_+^{(q)} \qquad \text{and} \qquad \hat{\mathbf{b}}_+^{(q)} = \hat{\mathbf{T}}_-^{(p,q)} \hat{\mathbf{a}}_-^{(p)} + \hat{\mathbf{R}}_+^{(p,q)} \hat{\mathbf{a}}_+^{(q)}. \tag{39}$$

The reflection and transmission matrices for $\Omega_{p,q}$ with Ω_{q+1} appended to its right-hand side, $\hat{\mathbf{R}}_\pm^{(p,q+1)}$ and $\hat{\mathbf{T}}_\pm^{(p,q+1)}$, can be calculated from $\hat{\mathbf{R}}_\pm^{(p,q)}$, $\hat{\mathbf{T}}_\pm^{(p,q)}$, $\hat{\mathbf{R}}_\pm^{(q+1)}$ and $\hat{\mathbf{T}}_\pm^{(q+1)}$ via

$$\mathbf{R}_-^{(p,q+1)} = \mathbf{R}_-^{(p,q)} + \mathbf{T}_+^{(p,q)} \left(\mathbf{I} - \mathbf{R}_-^{(q+1)} \mathbf{R}_+^{(p,q)} \right)^{-1} \mathbf{R}_-^{(q+1)} \mathbf{T}_-^{(p,q)}, \tag{40a}$$

$$\mathbf{T}_+^{(p,q+1)} = \mathbf{T}_+^{(p,q)} \left(\mathbf{I} - \mathbf{R}_-^{(q+1)} \mathbf{R}_+^{(p,q)} \right)^{-1} \mathbf{T}_+^{(q+1)} \tag{40b}$$

$$\mathbf{R}_+^{(p,q+1)} = \mathbf{R}_+^{(q+1)} + \mathbf{T}_-^{(q+1)} \left(\mathbf{I} - \mathbf{R}_+^{(p,q)} \mathbf{R}_-^{(q+1)} \right)^{-1} \mathbf{R}_+^{(p,q)} \mathbf{T}_+^{(q+1)}, \tag{40c}$$

$$\text{and} \qquad \mathbf{T}_-^{(p,q+1)} = \mathbf{T}_-^{(q+1)} \left(\mathbf{I} - \mathbf{R}_+^{(p,q)} \mathbf{R}_-^{(q+1)} \right)^{-1} \mathbf{T}_-^{(p,q)}, \tag{40d}$$

where $\mathbf{I}$ is the identity matrix of dimension $2J_\mathrm{i} + J_\mathrm{r} - 1$. These relations are derived from the scattering relations for an individual region (35), on the basis that (i) the outgoing wave field on the right-hand side of cylinder q is the incoming field on the left-hand side of cylinder $q + 1$, and (ii) the outgoing field on the left-hand side of cylinder $q + 1$ is the incoming field on the right-hand side of cylinder q, i.e. $\hat{\mathbf{a}}_-^{(q+1)} = \hat{\mathbf{b}}_+^{(q)}$ and $\hat{\mathbf{a}}_+^{(q)} = \hat{\mathbf{b}}_-^{(q+1)}$. Versions of relations (40) have been used by Botten et al. (2004),

Peter and Meylan (2009) and Bennetts (2011), among others, for electromagnetic, water wave and acoustic problems, respectively.

The reflection and transmission matrices $\hat{\mathbf{R}}_{\pm}^{(1,n)}$ and $\hat{\mathbf{T}}_{\pm}^{(1,n)}$ for $n = 1, \ldots, N$ are obtained by beginning with the leftmost region, Ω_1, recursively appending the next region to the right and applying Eqns. (40). The process is initialised with the identities $\hat{\mathbf{R}}_{\pm}^{(1,1)} = \hat{\mathbf{R}}_{\pm}^{(1)}$ and $\hat{\mathbf{T}}_{\pm}^{(1,1)} = \hat{\mathbf{T}}_{\pm}^{(1)}$. Similarly, the reflection and transmission matrices $\hat{\mathbf{R}}_{\pm}^{(n,N)}$ and $\hat{\mathbf{R}}_{\pm}^{(n,N)}$ for $n = 1, \ldots, N$ are obtained by beginning at the rightmost region, Ω_N, then recursively appending the next region to the left and applying similar equations to (40) for region $\Omega_{p,q}$ with Ω_{p-1} appended to its left-hand side.

The sampled amplitude functions throughout the array are obtained from the reflection and transmission matrices via

$$\hat{\mathbf{b}}_{+}^{(n)} = \left(\mathbf{I} - \hat{\mathbf{R}}_{+}^{(1,n)}\hat{\mathbf{R}}_{-}^{(n+1,N)}\right)^{-1}\left(\hat{\mathbf{T}}_{-}^{(1,n)}\hat{\mathbf{a}}_{-}^{(1)} + \hat{\mathbf{R}}_{+}^{(1,n)}\hat{\mathbf{T}}_{+}^{(n+1,N)}\hat{\mathbf{a}}_{+}^{(N)}\right) \tag{41a}$$

$$\text{and} \qquad \hat{\mathbf{a}}_{+}^{(n)} = \left(\mathbf{I} - \hat{\mathbf{R}}_{-}^{(n+1,N)}\hat{\mathbf{R}}_{+}^{(1,n)}\right)^{-1}\left(\hat{\mathbf{R}}_{-}^{(n+1,N)}\hat{\mathbf{T}}_{-}{}^{(1,n)}\hat{\mathbf{a}}_{-}^{(1)} + \hat{\mathbf{T}}_{+}{}^{(n+1,N)}\hat{\mathbf{a}}_{+}^{(N)}\right) \tag{41b}$$

for $n = 1, \ldots, N$. The vectors $\hat{\mathbf{a}}_{-}^{(1)}$ and $\hat{\mathbf{a}}_{+}^{(N)}$ are, respectively, the sampled directional spectra for the prescribed rightward and leftward propagating/decaying components of the ambient incident wave field, $\hat{A}_{\mathrm{am}-} = \hat{A}_{-}^{(1)}$ and $\hat{A}_{\mathrm{am}+} = \hat{A}_{+}^{(N)}$, defined via

$$\phi_{\mathrm{am}} = \int_{\Gamma_-} \hat{A}_{\mathrm{am}-}(\chi)\hat{\varphi}^{(1)}(x, y : \chi)\ \mathrm{d}\chi + \int_{\Gamma_+} \hat{A}_{\mathrm{am}+}(\chi)\hat{\varphi}^{(N)}(x, y : \chi)\ \mathrm{d}\chi. \tag{42}$$

Bennetts and Squire (2009) originally presented equivalent expressions to (41) for a problem involving multiple rows of floating bodies. Their expressions contained typographical errors, which are corrected above.

Calculation of the amplitude functions completes the solution process. Due to the recursive nature of the method, the computational cost increases linearly with the number of cylinders in the array, compared to the cubic increase for the standard interaction theory based on Graf's addition formulae (see the discussion in Montiel et al., 2016).

4 Damping of resonant loads

For the unperturbed problem, set the subregions Ω_n to have identical widths and be centred around the cylinders they contain, i.e. the $x_{n\pm} = x_n \pm d/2$ are the midpoints between adjacent cylinders. Therefore, the reflection and transmission kernels for the subregions are identical, and are denoted

$$\hat{\mathbf{R}}_{\pm} \equiv \hat{\mathbf{R}}_{\pm}^{(1)} = \cdots = \hat{\mathbf{R}}_{\pm}^{(N)} \qquad \text{and} \qquad \hat{\mathbf{T}}_{\pm} \equiv \hat{\mathbf{T}}_{\pm}^{(1)} = \cdots = \hat{\mathbf{T}}_{\pm}^{(N)}. \tag{43}$$

Due to symmetry $\hat{\mathbf{R}}_{+} = \hat{\mathbf{R}}_{-}$ and $\hat{\mathbf{T}}_{+} = \hat{\mathbf{T}}_{-}$, although this is not a requirement for the following analysis.

Let the transfer matrix, $\mathbf{P}$, which maps the amplitude functions on the left-hand side of a subregion to the amplitude functions on the right-hand side, be defined by

$$\begin{pmatrix} \hat{\mathbf{b}}_{+}^{(n)} \\ \hat{\mathbf{a}}_{+}^{(n)} \end{pmatrix} = \mathbf{P}\begin{pmatrix} \hat{\mathbf{a}}_{-}^{(n)} \\ \hat{\mathbf{b}}_{-}^{(n)} \end{pmatrix} \qquad \text{and} \qquad \mathbf{P} = \begin{pmatrix} \hat{\mathbf{T}}_{-} - \hat{\mathbf{R}}_{+}\hat{\mathbf{T}}_{+}^{-1}\hat{\mathbf{R}}_{-} & \hat{\mathbf{R}}_{+}\hat{\mathbf{T}}_{+}^{-1} \\ \hat{\mathbf{T}}_{+}^{-1}\hat{\mathbf{R}}_{-} & \hat{\mathbf{T}}_{+}^{-1} \end{pmatrix}. \tag{44}$$

The spectrum of the transfer matrix determines the properties of the unperturbed array. Fig. 6(a) shows an example of the eigenvalues $\lambda = \lambda_i$ $(i = 1, \ldots, 4J_{\mathrm{i}} + 2J_{\mathrm{r}} - 2)$ of the transfer matrix in the complex plane. The example problem considered is the resonant case Maniar and Newman (1997) identified for $N = 100$ cylinders, at frequency $kd = 2.78142$ ($kd/\pi \approx 0.88535$). The eigenvalues appear

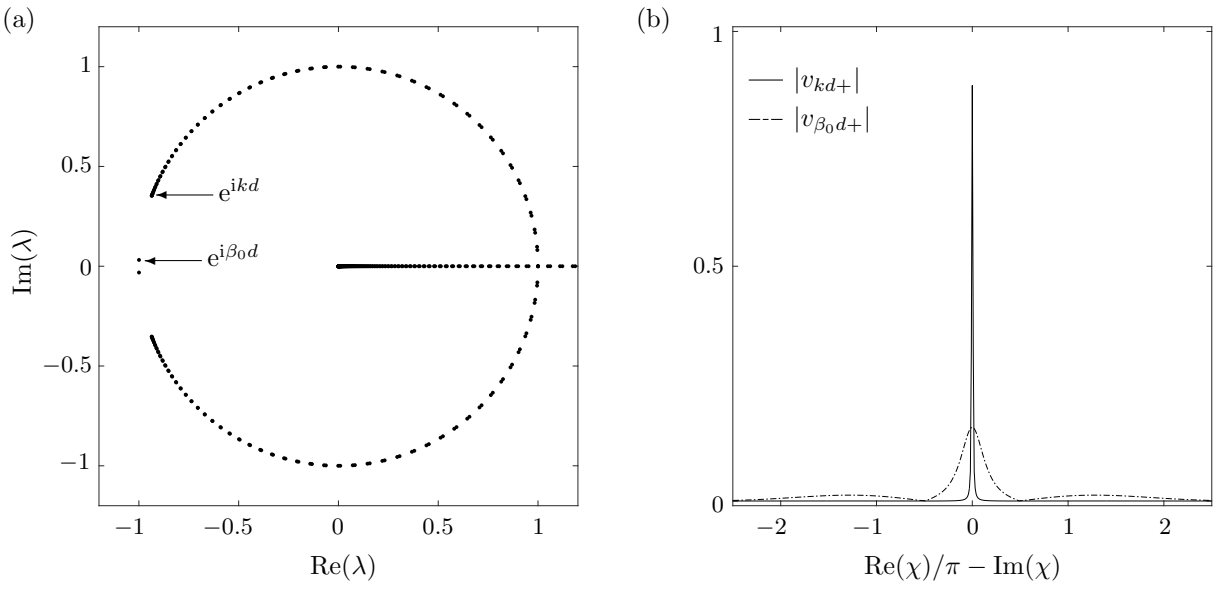

Figure 6: Spectrum of transfer matrix $\mathbf{P}$, defined in Eqn. (44), for $a/d = 0.25$ at the resonant frequency for the 100-cylinder array, $kd/\pi \approx 0.88535$. (a) Eigenvalues λ in the complex plane, with eigenvalues supporting head-on incidence in the positive x-direction, $\mathrm{e}^{\mathrm{i}kd}$, and the Rayleigh–Bloch mode propagating in the positive x-direction, $\mathrm{e}^{\mathrm{i}\beta_0 d}$, indicated. (b) The moduli of the corresponding eigenfunctions associated to rightward propagating/decaying motions, v_{kd+} and $v_{\beta_0 d+}$, respectively, as functions of the spectral parameter χ.

in reciprocal pairs, i.e. for $|\lambda| = 1$ if $\mathrm{e}^{\mathrm{i}\arg(\lambda)}$ is an eigenvalue then so is $\mathrm{e}^{-\mathrm{i}\arg(\lambda)}$, and for $\arg(\lambda) = 0$ if $|\lambda|$ is an eigenvalue then so is $1/|\lambda|$. Repeated eigenvalues relate to symmetric and antisymmetric eigenfunctions with respect to χ.

The eigenvalues forming the backwards $\subset$-shape on the unit circle are the discrete approximation of the continuous spectrum, corresponding to solutions in which wave energy propagates to the far field. In the infinite-array setting, these are solutions forced by a plane ambient incident wave. The angle of the ambient incident wave with respect to the x-axis, ψ_{am}, is related to the argument of the eigenvalue via $\arg(\lambda) = kd\cos(\psi_{\mathrm{am}})$. Therefore, the eigenvalues at $\lambda = 1$ correspond to incident waves normal to the array, propagating parallel to the y-axis. The eigenvalues at the tips of the backwards $\subset$-shape correspond to forcing at grazing incidence, i.e. parallel to the x-axis. The eigenvalue at the upper tip, which is labelled $\mathrm{e}^{\mathrm{i}kd}$, propagates rightwards. The eigenvalue at the lower tip, $\mathrm{e}^{-\mathrm{i}kd}$ (not labelled), propagates leftwards.

The subset of eigenvalues on the positive real axis form the discrete approximation to the continuous spectrum, generalised to forcing waves that decay exponentially. Eigenvalues smaller than unity decay rightwards, and eigenvalues greater than unity decay leftwards. Note that the set of eigenvalues greater than unity extends beyond the figure limits.

The pair of eigenvalues on the unit circle closest to negative unity correspond to Rayleigh–Bloch wave modes. These eigenvalues are denoted $\mathrm{e}^{\pm\mathrm{i}\beta_0 d}$, where $\beta_0 \in \mathbb{R}^+$ is the Rayleigh–Bloch wave number. They form the discrete spectrum, i.e. they correspond to solutions for which wave energy decays with distance away from the array. The eigenvalue in the upper half of the complex plane, which is labelled $\mathrm{e}^{\mathrm{i}\beta_0 d}$, propagates rightwards along the array, and the eigenvalue in the lower half of the complex plane, $\mathrm{e}^{-\mathrm{i}\beta_0 d}$, propagates leftwards. As these eigenvalues are separated from the $\subset$-shape $\beta_0 > k$, confirming that the Rayleigh–Bloch waves are shorter than the waves in the surrounding open water.

The definitions of continuous and discrete spectra used here are in terms of quasi-periodicities of

possible solutions for a given frequency. This differs from, for example, Porter and Evans (1999), who define the spectra in terms of frequencies at which solutions exist for a given quasi-periodicity. In simple terms, the spectral parameter here relates to the directional spectrum, whereas in Porter and Evans (1999) and others it relates to the frequency spectrum.

Fig. 6(b) shows the moduli of the rightward-propagating/decaying components of the eigenfunctions, $v_{kd+}(\chi)$ and $v_{\beta_0 d+}(\chi)$, associated to the labelled eigenvalues $\mathrm{e}^{\mathrm{i}kd}$ and $\mathrm{e}^{\mathrm{i}\beta_0 d}$, respectively. The eigenfunctions are approximated using the eigenvectors associated to the eigenvalues, and are normalised so that their L_2-norm is unity. The eigenfunction v_{kd} displays a sharp spike centred at $\chi = 0$. This is an approximation of a Dirac delta function, corresponding to the plane ambient incident wave in the infinite-array problem. In contrast, the eigenfunction $v_{\beta_0 d}$ is smooth, indicating that it is an unforced solution of the infinite-array problem. Its dominant energy is spread around $\chi = 0$, and it has sidebands spread onto the complex branches ($|\mathrm{Re}(\chi)/\pi - \mathrm{Im}(\chi)| > 1$).

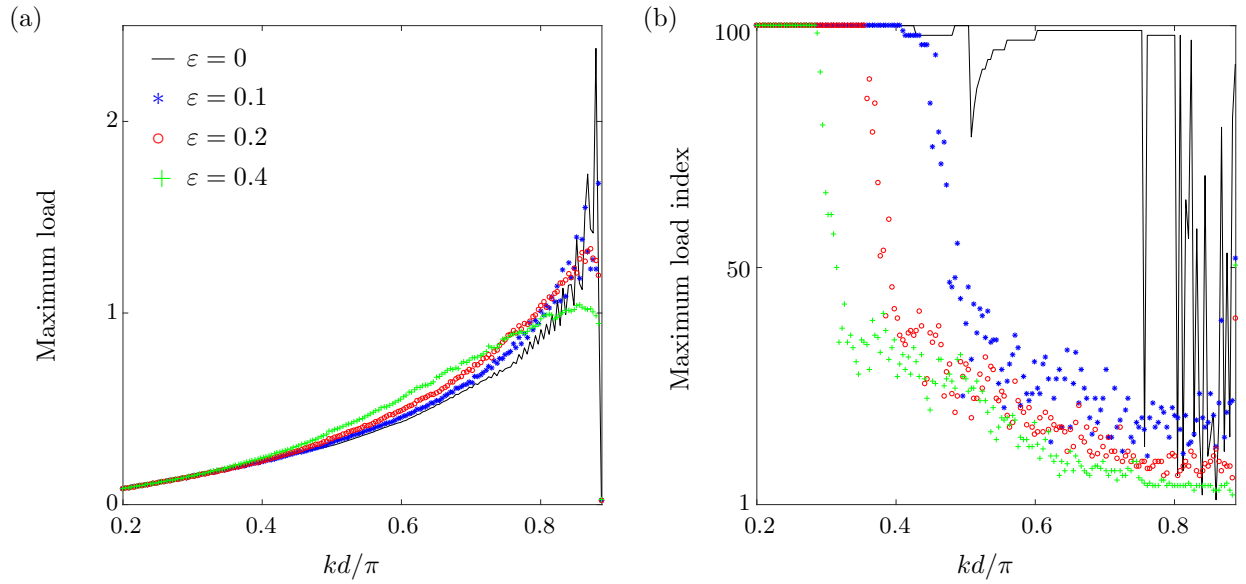

Figure 7: (a) As in Fig. 1 but for a Rayleigh–Bloch ambient incident wave. (b) Corresponding indices of the cylinders experiencing the maximum loads.

To simplify the analysis, the ambient incident wave field is set to be the rightward-propagating Rayleigh–Bloch mode, i.e. $\hat{A}_{\mathrm{am}-} = v_{\beta_0 d}$ and $\hat{A}_{\mathrm{am}+} = 0$. Fig. 7(a) shows the maximum (normalised) load on a 100-cylinder array, as a function of frequency, kd/π, for different perturbation strengths, ε. It is equivalent to Fig. 1 for the Rayleigh–Bloch incident wave rather than the plane incident wave, with the frequency range truncated due to the cut-off at $kd/\pi \approx 0.88574$. For frequencies immediately beyond the cut-off, the Rayleigh–Bloch wave numbers become complex and the Rayleigh–Bloch wave decays along the array (as identified by Thompson et al., 2008).

For the unperturbed problem, the Rayleigh–Bloch incident wave excites a resonance at the same frequency as the plane incident wave. This is logical, as the resonance produced by a plane incident wave is associated to excitation of the Rayleigh–Bloch modes (as explained in § 1, cf. Thompson et al., 2008). Moreover, in an identical fashion to the plane-wave case, perturbations damp the resonance for the Rayleigh–Bloch incident wave field.

Fig. 7(b) shows the indices of the cylinders at which the maximum load is attained. For low frequencies, the maximum is attained at the farthest cylinder from the source of the incident wave field (the right-hand end of the array, $n = 100$), due to cylinders refracting the rightward-propagating incident wave energy in towards the array (Maniar and Newman, 1997). This low-frequency behaviour

is consistent for the different perturbation strengths, as the perturbations are small in comparison to the wavelength, $2\pi/k$, in this regime. For the unperturbed array, the maximum load is attained at the right-hand end of the array up to $kd/\pi \approx 0.4$–0.5. As the frequency increases beyond this limit, the location of the maximum begins to jump around erratically. For the perturbed arrays, the maximum load departs the right-hand end of the array for lower frequencies than the unperturbed array, with the departure frequency decreasing as the perturbation strength increases. The location of the maximum then transitions relatively smoothly towards the front cylinder (left-hand end of the array, $n = 1$), as frequency increases.

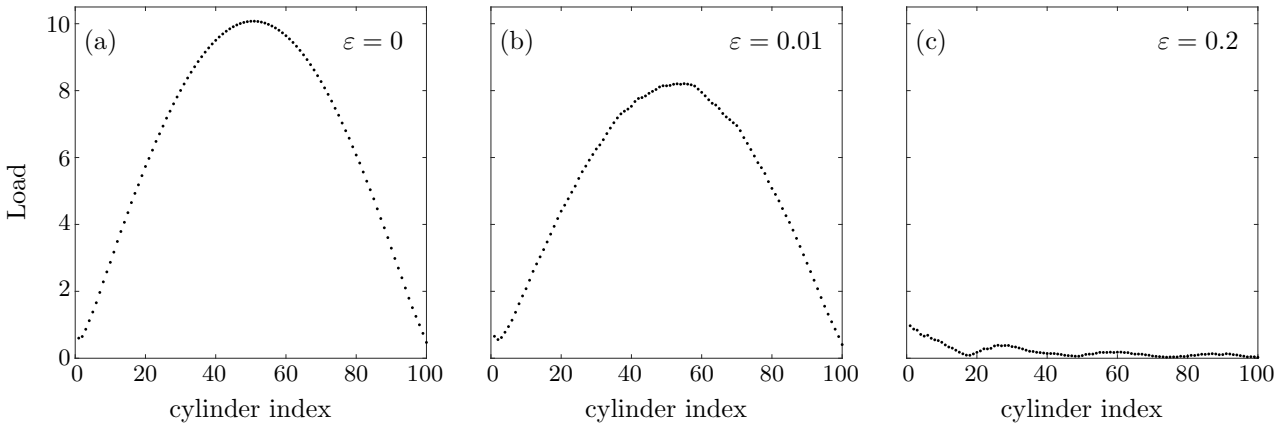

Figure 8: Example realisations of load profiles on 100-cylinder arrays for $a/d = 0.25$, $kd/\pi \approx 0.88535$, and (a) no perturbation, (b) perturbation strength $\varepsilon = 0.01$, and (c) $\varepsilon = 0.2$.

Fig. 8 shows example profiles of the loads on the array at the resonance frequency $kd/\pi \approx 0.88535$. It shows the profile for the unperturbed array and for two random realisations of the perturbed array, for perturbation strengths $\varepsilon = 0.01$ and 0.2. The profile for the unperturbed array is qualitatively identical to that presented by Maniar and Newman (1997) for a plane incident wave — it is an approximately symmetric hump, with the maximum load attained at the centre ($n = 51$), due to coherence between strongly excited rightward- and leftward-propagating Rayleigh–Bloch modes (Thompson et al., 2008). The weak perturbation ($\varepsilon = 0.01$) preserves the near symmetry but slightly shortens the length of the resonant hump and damps the maximum load. The strong perturbation ($\varepsilon = 0.2$) fundamentally changes the qualitative properties of the profile, eliminating symmetry and resonance altogether. The profile attenuates from the front of the array to the rear, with accompanying oscillations, indicating a localised state has been reached.

5 Localisation of Rayleigh–Bloch waves

For the unperturbed array forced by a Rayleigh–Bloch ambient incident wave, the wave field along the array is dominated by rightward- and leftward-propagating Rayleigh–Bloch modes. For a perturbed array, it is hypothesised that, similarly, the wave field is dominated by perturbed Rayleigh–Bloch modes, with complex-valued wave number $\beta_+(\varepsilon) \in \mathbb{R}_+ + \mathrm{i}\mathbb{R}_+$ for the rightward-propagating mode and $\beta_-(\varepsilon) \in \mathbb{R}_- + \mathrm{i}\mathbb{R}_-$ for the leftward-propagating mode. It is expected that $\beta_- \approx -\beta_+$, on average at least, due to symmetry of the perturbations, and for the unperturbed array $\beta_\pm(0) = \pm\beta_0$. The change in the real parts of the wave numbers, with respect to the unperturbed Rayleigh–Bloch wave numbers, induces phase shifts in the modes, and the introduction of imaginary components produces attenuation of the modes, resulting in localisation for sufficiently large attenuation rates.

The perturbed wave numbers, $\beta_\pm$, are extracted from wave fields for the perturbed arrays, using a

version of the approach proposed by Bennetts and Peter (2013). For each realisation of the perturbed array, the wave fields are calculated for

(i) a rightward-propagating Rayleigh–Bloch incident wave ($\hat{A}_{\mathrm{am}-} = v_{\beta_0 d+}$ and $\hat{A}_{\mathrm{am}+} = 0$, as in § 4),

(ii) and a leftward-propagating Rayleigh–Bloch incident wave ($\hat{A}_{\mathrm{am}-} = 0$ and $\hat{A}_{\mathrm{am}+} = v_{-\beta_0 d-} = v_{\beta_0 d+}$).

The rightward- and leftward-propagating directional amplitude functions along the array for these wave fields are denoted

$$\xi^{(n)}_{\beta_\pm d} = \hat{B}^{(n-1)}_{+} = \hat{A}^{(n)}_{-} \qquad \text{and} \qquad \zeta^{(n)}_{\beta_\pm d} = \hat{A}^{(n-1)}_{+} = \hat{B}^{(n)}_{-} \qquad \text{for} \qquad n = 1, \ldots, N+1, \tag{45}$$

respectively, where the undefined amplitude functions at the boundaries of the array are replaced by the equivalent functions of the ambient incident wave fields, i.e. $\hat{B}^{(0)}_{+} \equiv \hat{A}_{\mathrm{am}-}$ and $\hat{B}^{(N+1)}_{-} \equiv \hat{A}_{\mathrm{am}+}$. The hypothesis that the wave fields are dominated by perturbed Rayleigh–Bloch modes is translated into the ansatzes

$$\xi^{(n)}_{\beta_\pm d} \approx a^{(\xi)}_{\pm} \mathrm{e}^{\mathrm{i}\beta_+ dn} v_{\beta_+ d+} + b^{(\xi)}_{\pm} \mathrm{e}^{\mathrm{i}\beta_- d(N+1-n)} v_{\beta_- d+} \tag{46a}$$

$$\text{and} \qquad \zeta^{(n)}_{\beta_\pm d} \approx a^{(\zeta)}_{\pm} \mathrm{e}^{\mathrm{i}\beta_+ dn} v_{\beta_+ d-} + b^{(\zeta)}_{\pm} \mathrm{e}^{\mathrm{i}\beta_- d(N+1-n)} v_{\beta_- d-}, \tag{46b}$$

where $a^{(\bullet)}_{\pm}(\varepsilon)$ and $b^{(\bullet)}_{\pm}(\varepsilon)$ are coefficients/amplitudes, $v_{\beta_\pm d+}$ is the component of the eigenfunction associated to $\beta_\pm$ propagating/decaying rightwards, and $v_{\beta_\pm d-}$ is the component propagating/decaying leftwards.

Ansatzes (46) are combined, as in Bennetts and Peter (2013), to produce the expression

$$\mathrm{eig}\Big(\mathbf{M}^{(n)}\Big) = \{\mathrm{e}^{\mathrm{i}\beta_+ dn}, \mathrm{e}^{\mathrm{i}\beta_- dn}\} \qquad \text{for} \qquad n = 1, \ldots, N, \tag{47a}$$

$$\text{where} \qquad \mathbf{M}^{(n)} = \mathbf{M}^{(n,N+1)} \mathrm{inv}\Big(\mathbf{M}^{(1,N+1-n)}\Big), \qquad \mathbf{M}^{(p,q)} = \begin{pmatrix} \xi^{(p)}_{\beta_+ d}(0) & \xi^{(q)}_{\beta_- d}(0) \\ \zeta^{(p)}_{\beta_+ d}(0) & \zeta^{(q)}_{\beta_- d}(0) \end{pmatrix}, \tag{47b}$$

and $\mathrm{eig}(\cdot)$ denotes the set of eigenvalues of the included matrix. The values of the amplitude functions corresponding to wave components propagating parallel to the x-axis only are used because the ansatzes essentially reduce the problem to a single dimension.

Fig. 9 shows an example of logarithms of the eigenvalues of the matrix $\mathbf{M}^{(n)}$, as a function of cylinder index n, for a 100-cylinder array with perturbation strength $\varepsilon = 0.2$ at the resonant frequency for the unperturbed array, $kd/\pi \approx 0.88535$. The eigenvalues are separated into real and imaginary parts (left- and right-hand panels, respectively), and those corresponding to β_+ and β_- (top and bottom panels, respectively). The results are the means of ensembles of 500 randomly generated realisations of the perturbations.

The log-eigenvalue profiles are approximately linear — noise is visible in the imaginary parts but not in the real parts, which are dominated by the eigenvalues of the underlying unperturbed array. Straight-line fits are overlaid on the profiles, from which the non-dimensional Rayleigh–Bloch wave numbers, $\beta_\pm d$, are extracted as the slopes. The fits are made to the interior of the profiles only, to avoid contamination by local effects of the array ends, just visible in the imaginary parts. The extracted Rayleigh–Bloch wave numbers display the expected symmetry (to three decimal places), with $\beta_+ d \approx 3.02058 + 0.01536\mathrm{i}$ and $\beta_- d \approx -3.02055 - 0.01548\mathrm{i}$.

Extracting array wave numbers (in this case Rayleigh–Bloch wave numbers) from mean log-eigenvalue profiles is more stable than Bennetts and Peter (2013)'s method of extracting array wave numbers from log-eigenvalue profiles of individual realisations and then averaging. The Rayleigh–Bloch wave numbers are not those of the effective (mean) wave field, as the amplitudes and phases are separated prior to averaging.

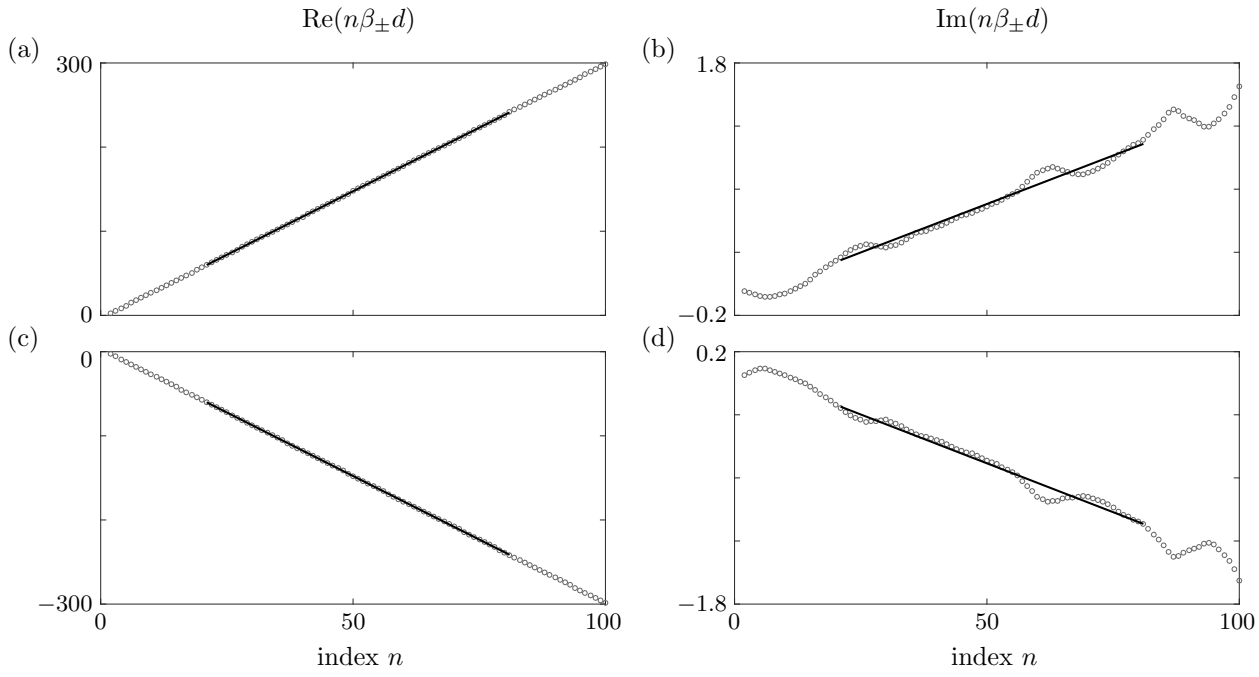

Figure 9: Eigenvalues of matrix $M^{(n)}$, given in Eqn. (47), corresponding to rightward-propagating (top panels, a,b) and leftward-propagating (bottom panels, c,d) Rayleigh–Bloch modes for $a/d = 0.25$, $kd/\pi \approx 0.88535$ and $\varepsilon = 0.2$. Left-hand panels (a,c) show the real parts of the logarithms of the modes (phases) and the right-hand panels (b,d) show the imaginary parts (attenuation), with means of an ensemble of 500 simulations (○) overlaid by the straight-line fits (–) used to extract the Rayleigh–Bloch wave numbers.

Fig. 10 shows the extracted wave numbers as functions of perturbation strength for the resonant frequency, and using ensembles of 100 realisations for each perturbation strength. The real parts (phases) are shown as relative deviations from the Rayleigh–Bloch wave numbers of the unperturbed array,

$$\Delta\mathrm{Re}(\beta_\pm d) = \frac{\mathrm{Re}(\beta_\pm d) \mp \beta_0 d}{\beta_0 d}, \tag{48}$$

in the left-hand panels, with the imaginary parts (attenuation rates) shown in the right-hand panels. Wave numbers supporting rightward-propagating/attenuating modes are shown in the top panels, with those for the leftward-propagating/attenuating modes in the bottom panels. Results are shown for 100-cylinder arrays and 200-cylinder arrays.

The results again show the expected symmetry $\beta_- \approx -\beta_+$. The phase changes are similar for the 100- and 200-cylinder arrays, indicating that the real parts of the Rayleigh–Bloch wave numbers do not depend on array length (beyond $N = 100$ at least). Deviations between the phases for the two array lengths are evident for weak perturbations, approximately $\log_{10}\varepsilon < -1.5$ ($\varepsilon < 0.03162$), with the phase changes approximately zero in this regime for the 200-cylinder arrays, i.e. $\beta_\pm(\varepsilon) \approx \pm\beta_0$ for $\varepsilon \ll 1$ as expected, but being a small finite value for the 100-cylinder array. The errors for the 100-cylinder array are due to this being an insufficiently long interval to average out the presence of oscillations caused by the circular wave fields generated at the array ends, which compromise the validity of ansatzes (46). Stronger perturbations, $\log_{10}\varepsilon > -1.5$, clearly reduce the modulus of the phase of the Rayleigh–Bloch wave numbers, with the reduction steadily increasing as the perturbation strength increases.

In the weak-perturbation regime, $\log_{10}\varepsilon < -1.5$, deviations between the two arrays lengths are

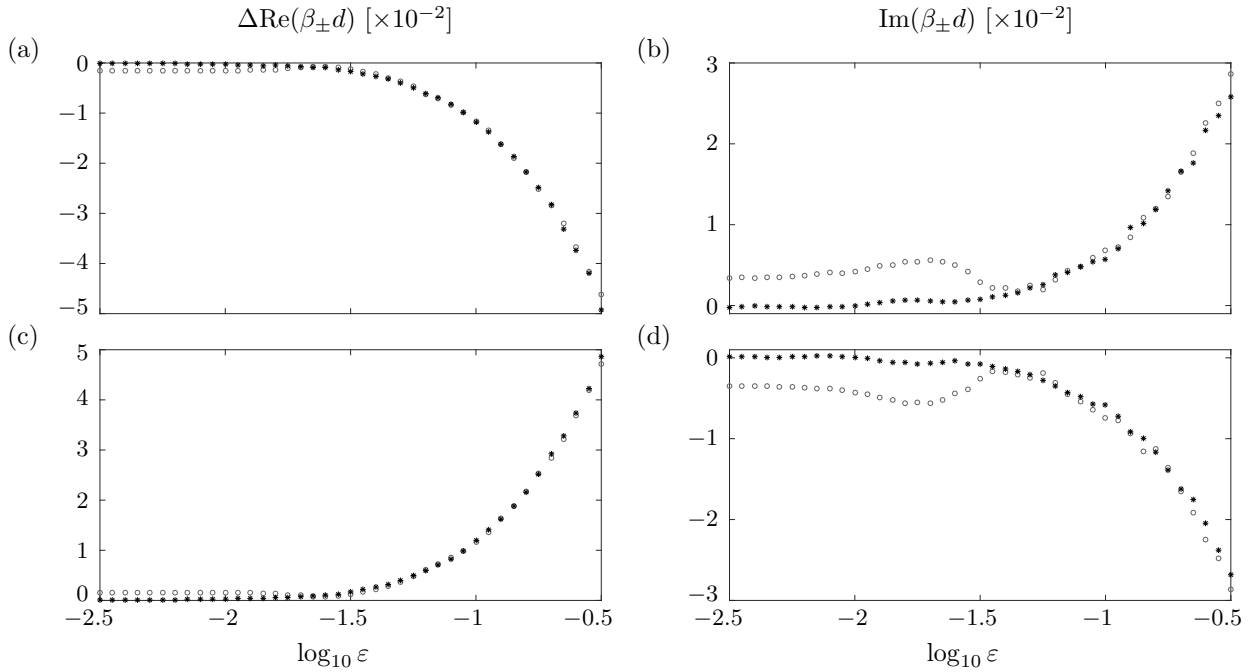

Figure 10: Rayleigh–Bloch wave numbers as functions of disorder for $a/d = 0.25$ and $kd/\pi \approx 0.88535$, calculated using a 100-cylinder array ($\circ$) and a 200-cylinder array ($*$). Top panels (a,b) show results for the rightward-propagating/attenuating Rayleigh–Bloch mode, and the bottom panels (c,d) show the leftward-propagating/attenuating mode. Left-hand panels (a,c) show the phase changes relative to the zero-perturbation case, and the right-hand panels (b,d) show the attenuation rates.

exacerbated for the attenuation rates, as the attenuation is negligible so that the oscillations caused by the circular wave fields dominate the imaginary-component profiles. The 200-cylinder array provides attenuation rates that are approximately zero for very weak perturbations, approximately $\log_{10}\varepsilon < -2$ ($\varepsilon < 0.01$), as expected, whereas attenuation rates for the 100-cylinder array are visibly non-zero in this regime. For stronger perturbations, $\log_{10}\varepsilon > -1.5$, the moduli of the attenuations rates increase with increasing perturbation strength and the attenuation rates for the 100-cylinder array rapidly transition to agreement with those of the 200-cylinder array. This marks the regime in which attenuation dominates the profiles of the imaginary components of the eigenvalues of $M^{(n)}$.

Fig. 11(a) shows the corresponding maximum load on the 200-cylinder array produced by a rightward-propagating Rayleigh–Bloch ambient incident wave field, and the load on the front cylinder ($n = 1$), as functions of perturbation strength. The resonance in the maximum load for the unperturbed 200-cylinder array at $kd/\pi \approx 0.88535$ manifests as two symmetric humps in the load profile, where each hump is almost identical to that shown in Fig. 8(a) for the 100-cylinder array. (A stronger, single-hump resonance for the 200-cylinder array, analogous to that Fig. 8(a) shows for the 100-cylinder array, is obtained at a slightly higher frequency.)

For weak perturbations, $\log_{10}\varepsilon < -1.5$, resonance in the maximum load is damped, as indicated in Fig. 8(b) for the 100-cylinder array, with the damping gradually increasing as the perturbation strength increases. Fig. 11(b) shows an individual load profile in the weak-perturbation regime, with $\log_{10}\varepsilon = -2$, for which $\beta_{\pm}d \approx \pm 3.109 \pm 0.000\mathrm{i}$. The profile is similar to the two-hump resonant profile occurring for the unperturbed array at this frequency, but with the resonances damped and the hump lengths reduced. The load profile for the unperturbed array with frequency $kd/\pi \approx 0.88532$, for which $\beta_0 d \approx 3.109$, is superimposed on the panel. It is almost identical to the profile for the perturbed array, indicating that a weakly-perturbed array acts like an unperturbed array with a slightly shorted

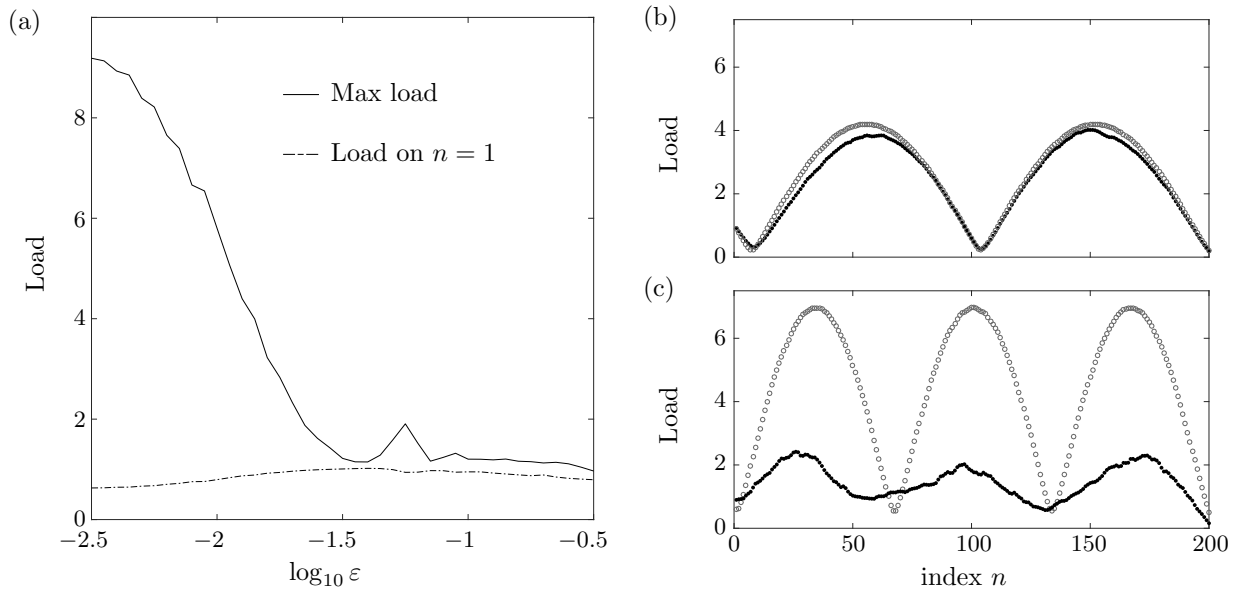

Figure 11: (a) Maximum load (–) and load on the first cylinder (---), caused by a rightward-propagating Rayleigh–Bloch ambient incident wave on a 200-cylinder array for $a/d = 0.25$ and $kd/\pi \approx 0.88535$, as functions of disorder. (b) A corresponding load-profile realisation for $\log_{10}\varepsilon = -2$ (•), and the profile for the unperturbed problem with $kd/\pi \approx 0.88532$ (◦). (c) As in (b) but for $\log_{10}\varepsilon = -1.25$ (•), and $kd/\pi \approx 0.88487$ (◦).

cylinder spacing and/or to slightly shifted forcing. (Alternatively, a similar profile can be obtained at the resonant frequency by increasing the number of cylinders in the unperturbed array to $N = 204$.)

For stronger perturbations, $\log_{10}\varepsilon > -1.5$, the maximum load is approximately equal to the load on the front cylinder, as the attenuation rates are, in general, sufficiently large to produce a localised states, as shown in Fig. 8(c) for the 100-cylinder array. A weak resonance in the maximum load around $\log_{10}\varepsilon = -1.25$ ($\varepsilon \approx 0.05623$) causes it to deviate away from the load on the front cylinder. Fig. 11(c) shows an individual load profile for $\log_{10}\varepsilon = -1.25$, for which $\beta_\pm \approx \pm 3.094 \pm 0.003\mathrm{i}$, with the load profile for the unperturbed array at frequency $kd/\pi \approx 0.88487$ superimposed, for which $\beta_0 \approx 3.094$. The profile for the unperturbed array is resonant, as indicated by the three humps and the symmetry of the profile, although it is a weaker resonance than the two-hump resonance at $kd/\pi \approx 0.88535$. The three humps are visible in the profile for the perturbed array, driving the resonance in the maximum load around $\log_{10}\varepsilon = -1.25$. However, attenuation produced by the imaginary component of the Rayleigh–Bloch wave number significantly reduces the hump peaks, so that the resonance is weak.

6 Summary and conclusions

A new solution method has been presented for water-wave interactions with line arrays of bottom-mounted, surface-piercing cylinders, in which the wave field excited by an ambient incident wave is calculated recursively, so that the numerical cost increases only linearly with the number of cylinders in the array. The directional scattering kernels for a solitary cylinder, used in the method, identify the Rayleigh–Bloch modes responsible for causing resonant loads in the interior of the array. It was shown that Rayleigh–Bloch modes can be used as the ambient incident wave field to excite the resonant loads, considerably simplifying the analysis.

The method readily permits perturbations to be introduced into the array. It was shown that perturbations in the positions of the cylinders damp the resonant loads. Perturbations of order 1 % of

the cylinder spacing were shown to damp the resonance weakly. These perturbations produce phase shifts in the load profiles along the arrays, meaning the arrays respond in a similar fashion to an unperturbed array with slightly smaller cylinder spacings. Perturbations of order 10 % strongly damp the resonance. They result in the maximum load occurring close to the front of the array, with the loads generally diminishing with distance into the array.

The strong damping was associated to the localisation phenomenon. Perturbed Rayleigh–Bloch wave numbers were calculated for the perturbed arrays by combining wave fields excited by unperturbed Rayleigh–Bloch incident fields, for ensembles of randomly generated realisations of the perturbations. For perturbations of order 1 %, the perturbed Rayleigh–Bloch wave numbers remain approximately real, relating to the phase shifts in the load profiles, and the weak damping of the resonances. Perturbations of order 10 % produce imaginary components of appreciable magnitudes in the perturbed Rayleigh–Bloch wave numbers, attenuating the corresponding modes as they propagate along the arrays, so that the maximum load is attained close to the front of the array, and resulting in localisation if the attenuation rates are sufficiently large with respect to the array length.

It would be difficult to confirm the localisation predicted here experimentally, as it would have to be disentangled from the dissipative mechanisms inevitable in water-wave problems. For instance, the attenuation of the wave profile through the array found by Kagemoto et al. (2002), which they attribute to viscous dissipation, is, superficially, similar to attenuation signalling localisation. Although it is clearly not a localisation effect in this case (e.g. positional inaccuracies equivalent to perturbation strengths < 0.6 % are reported), viscous dissipation would still play a role for stronger perturbations. Analogous issues are inherent in many other phenomena where localisation is predicted (see the discussion in Weaver, 1990).

Acknowledgements

The Australian Research Council funds an early-career fellowship for LGB (DE130101571). The US Office of Naval Research funds a postdoctoral fellowship for FM (Award number N00014-131-0279). The University of Adelaide hosted MAP for a sabbatical, during which this work was accomplished. LGB and MAP acknowledge useful discussions with Richard Porter regarding Rayleigh–Bloch waves.

References

M. Belzons, E. Guazzelli, and O. Parodi. Gravity waves on a rough bottom: experimental evidence of one-dimensional localization. *J. Fluid Mech.*, 186:539–558, 1988. doi: 10.1017/S0022112088000266.

L. G. Bennetts. Wave attenuation through multiple rows of scatterers with differing periodicities. *SIAM J. Appl. Maths.*, 71(2):540–558, 2011.

L. G. Bennetts and M. A. Peter. Spectral analysis of wave propagation through rows of scatterers via random sampling and a coherent potential approximation. *SIAM J. Appl. Math.*, 73(4):1613—1633, 2013.

L. G. Bennetts and V. A. Squire. Wave scattering by multiple rows of circular ice floes. *J. Fluid Mech.*, 639:213–238, 2009.

L. G. Bennetts, M. A. Peter, and H. Chung. Absence of localisation in ocean wave interactions with a rough seabed in intermediate water depth. *Q. J. Mech. Appl. Math.*, 68:97–113, 2015.

Luke G Bennetts and Vernon A Squire. On the calculation of an attenuation coefficient for transects of ice-covered ocean. *Proc. R. Soc. A*, 2012. doi: 10.1098/rspa.00000000.

M V Berry and S Klein. Transparent mirrors: rays, waves and localization. *Eur. J. Phys.*, 18:222–228, 1997.

L. C. Botten, T. P. White, A. A. Asatryan, T. N. Langtry, C. M. de Sterke, and R. C. McPhedran. Bloch mode scattering matrix methods for modeling extended photonic crystal structures. I. Theory. *Phys. Rev. E*, 70:056606, 2004.

D. J. Colquitt, R. V. Craster, T. Antonakakis, and S. Guenneau. Rayleigh–Bloch waves along elastic diffraction gratings. *Proc. R. Soc. A*, 471:20140465, 2015. doi: 10.1098/rspa.2014.0465.

P. Devillard, B. Souillard, and F. Dunlop. Gravity waves on a channel with a random bottom. *J. Fluid Mech.*, 186:521–538, 1988.

D. V Evans and R. Porter. Trapping and near-trapping by arrays of cylinders in waves. *J. Eng. Maths.*, pages 149–179, 1999.

E. Guazzelli and E. Guyon. On the localization of shallow water waves by a random bottom. *J. Phys. Paris*, 44(20):837–841, 1983.

C. H. Hodges and J. Woodhouse. Vibration isolation from irregularity in a nearly periodic structure: Theory and measurements. *J. Acoust. Soc. Am.*, 74(3):894–905, 1983.

H. Kagemoto, M. Murai, M. Saito, B. Molin, and Š. Malenica. Experimental and theoretical analysis of the wave decay along a long array of vertical cylinders. *J. Fluid Mech.*, 456:113–135, 2002. doi: 10.1017/S0022112001007480.

C. M. Linton and M. McIver. The existence of Rayleigh-Bloch surface waves. *J. Fluid Mech.*, 470 (1994):1–5, 2002. doi: 10.1017/S0022112002002227.

C. M Linton, R. Porter, and I. Thompson. Scattering by a semi-infinite periodic array and the excitation of surface waves. *SIAM J. Appl. Math.*, 67(5):1233–1258, 2007.

H. D. Maniar and J. N. Newman. Wave diffraction by a long array of cylinders. *J. Fluid Mech.*, 339: 309–330, 1997.

P. A. Martin. *Multiple scattering: interaction of time-harmonic waves with N obstacles.* Cambridge University Press, 2006.

F. Montiel, V. A. Squire, and L. G. Bennetts. Evolution of directional wave spectra through finite regular and randomly-perturbed arrays of scatterers. *SIAM J. Appl. Maths.*, 75:DOI. 10.1137/140973906, 2015.

F. Montiel, V. A. Squire, and L. G. Bennetts. Attenuation and directional spreading of ocean wave spectra in the marginal ice zone. *J. Fluid Mech.*, 790:492–522, 2016. doi: 10.1017/jfm.2016.21.

M. A. Peter and M. H. Meylan. Water-wave scattering by a semi-infinite periodic array of arbitrary bodies. *J. Fluid Mech.*, 575:473–494, 2007.

M. A. Peter and M. H. Meylan. Water-wave scattering by vast field of bodies. *SIAM J. Appl. Maths.*, 70(5):1567–1586, 2009.

R. Porter and D. V. Evans. Rayleigh-Bloch surface waves along periodic gratings and their connection with trapped modes in waveguides. *J. Fluid Mech.*, 386:233–258, 1999.

P. Sheng. *Introduction to wave scattering, localisation and mesoscopic phenomena.* Springer, Berlin, 2nd edition, 2006.

A. Sommerfeld. *Partial differential equations in physics*, volume Vol. 1. Academic Press, 1949.

I. Thompson, C. M. Linton, and R. Porter. A new approximation method for scattering by long finite arrays. *Q. J. Mech. Appl. Math.*, 61(3):333–352, 2008.

R. L. Weaver. Anderson localization of ultrasound. *Wave Motion*, 12(2):129–142, 1990. doi: 10.1016/0165-2125(90)90034-2.